RSC Advances

PAPER

View Article Online
View Journal | View Issue

Cite this: *RSC Adv.*, 2020, **10**, 40291

Effects of Al-dopant at Ni or Co sites in $LiNi_{0.6}Co_{0.3}Ti_{0.1}O_2$ on interlayer slabs (Li–O) and intralayer slabs (TM–O) and their influence on the electrochemical performance of cathode materials

Wan Aida Hazwani Wan Azizan,[ab] Muhd Firdaus Kasim,*[ab] Kelimah Elong,[ab] Roshidah Rusdi,[ac] Rizuan Mohd Rosnan[d] and Norlida Kamarulzaman[c]

In order to satisfy the energy demands of the electromobility market, further improvements in cathode materials are receiving much attention, especially high energy density cathode materials for Li-ion batteries (LIBs). In this work, the self-propagating combustion (SPC) method is use to synthesise undoped $LiNi_{0.6}Co_{0.3}Ti_{0.1}O_2$ (LNCT), novel nano-sized Al-doped $LiNi_{0.6}Co_{0.3-x}Al_xTi_{0.1}O_2$ (LCA) and $LiNi_{0.6-x}Co_{0.3}Al_xTi_{0.1}O_2$ (LNA) ($x = 0.01$) cathode materials. LNCT, LCA and LNA were annealed at 700 °C for 24 h. Following the synthesis, the phase, chemical structure and purity of the materials were analysed using X-ray diffraction (XRD). Based on the XRD results, all materials exhibit a single-phase structure with rhombohedral layered structure. Based on the HRTEM and EDX results, all samples exhibit polyhedral-like shapes, while the Al-doped samples display smaller crystallite sizes compared to the undoped sample. As for the electrochemical performances, the initially discharged capacity of LCA (238.6 mA h g^{-1}) is higher than that of LNA (214.7 mA h g^{-1}) and LNCT (150.5 mA h g^{-1}). However, LNA has a lower loss of capacity after the 50th cycle compared to the LCA sample, which makes it a more excellent candidate for electrochemical applications. The main reason for the excellent electrochemical behaviour of LNA is due to lower cation mixing. Furthermore, Rietveld refinements reveal that the LNA sample has a longer atomic distance of Li–O and shorter TM–O in the cathode structure, which makes Li^+ ion diffusion more efficient, leading to excellent electrochemical performance. These findings further proved the potential of the novel nano cathode material of $LiNi_{0.6-x}Co_{0.3}Al_xTi_{0.1}O_2$ (LNA) to replace the existing commercialized cathode materials for rechargeable Li-ion batteries.

Received 30th August 2020
Accepted 22nd October 2020

DOI: 10.1039/d0ra07434a

rsc.li/rsc-advances

1. Introduction

Lately, most people prefer the use of portable electronic devices to aid in their daily routines. Hence, the need for a renewable energy storage system has increased in demand as it is crucial to run daily chores without a pause. Li-ion batteries are one of the preferred systems due to their properties, which include high energy densities, small self-discharge rate and no memory effect.[1] In any types of batteries, the cathode materials ensure the safety and performance of the batteries. A majority of Li-ion batteries use lithium cobalt dioxide ($LiCoO_2$) as their cathode material.[2,3] The $LiCoO_2$ cathode has well-ordered layers of crystal structure that makes the lithium extraction/insertion processes faster. For this very reason, $LiCoO_2$ was proven to yield good performance in the Li-ion battery industries with a theoretical specific capacity of 274 mA h g^{-1}.[4–6] Despite the proven capacity, the cobalt (Co) element in the $LiCoO_2$ materials is toxic, expensive and has low abundance. Thus, many researchers are trying to substitute the cobalt with another efficient element to produce a cathode material with similar or better performance than that of $LiCoO_2$.

A study on nickel (Ni) doping of $LiCoO_2$ was carried out, where $LiNiO_2$ was proven to be a better candidate to replace $LiCoO_2$.[7–12] $LiNiO_2$ was also found to possess a similar crystal structure and theoretical specific capacity to $LiCoO_2$. In fact, Ni-based materials have higher energy densities and are cheaper than Co-based materials.[7,13,14] Therefore, the Ni-based materials are favourable. Nevertheless, pure $LiNiO_2$ materials are not preferred.[12] This is due to the small differences in the atomic radii of Ni ions and Li ions; the Ni^{2+} ions (0.69 Å) tend to occupy Li^+ ion (0.76 Å) sites (cationic disorder) during the synthesis and delithiation, thus, preventing Li^+ ions from fixing at their original sites. Therefore,

[a]*Centre for Functional Materials and Nanotechnology, Institute of Science, Universiti Teknologi MARA, Level 3 Block C, 40450 Shah Alam, Selangor, Malaysia. E-mail: muhdfir@uitm.edu.my; Tel: +60-3-5544-4473, +60-17-356-9582*

[b]*School of Chemistry and Environment, Faculty of Applied Sciences, Universiti Teknologi MARA, 40450 Shah Alam, Selangor, Malaysia*

[c]*School of Physics and Materials Studies, Faculty of Applied Sciences, Universiti Teknologi MARA, 40450 Shah Alam, Selangor, Malaysia*

[d]*JEOL (MALAYSIA) Sdn. Bhd., 47301 Petaling Jaya, Selangor, Malaysia*

in order to avoid the cationic disorder, Ni was partially substituted with other transition or non-transition metals. However, the addition of a large amount of these non-transition metals is not encouraged since the inactivity of the metals will cause the reversible capacity of the batteries to become low.[15,16]

Among Ni-rich materials, $LiNi_{0.6}Co_{0.3}Ti_{0.1}O_2$ was fabricated by Baster *et al.* (2018) and it has attracted our attention due to the usage of Ti^{4+} to stabilize the structure.[17] This material is pure and single phase with the well-ordered hexagonal layered structure of the $R\bar{3}m$ space group and it also exhibits first cycle capacity of 100 mA h g^{-1} at a voltage maintained at an average value of ~4.2 V *vs.* Li/Li^+. However, this material possesses a quite big (micron) crystallite size that leads to a longer Li^+ pathway and small interfacial contact area with the liquid electrolyte. These properties prompted us to further adapt the material by doping aluminium (Al) into Co or Ni sites. According to some of the available literature,[10,11] Al-doped materials have a higher discharge capacity and improve the cycling stability of the materials due to its single oxidation state. Besides, Al is cheaper and less toxic compared Co and Ni, making the materials more cost-effective and greener.[18–20] Thus, novel nano-sized materials of Al-doped $LiNi_{0.6}Co_{0.3-x}Al_xTi_{0.1}O_2$ and $LiNi_{0.6-x}Co_{0.3}Al_xTi_{0.1}O_2$ ($x = 0.01$) were synthesised through a self-propagating combustion method. This method was chosen due to its short synthesis time where the formed product has a small and uniform crystallite size.[21–23] The performance of the synthesised materials was investigated in relation to their crystal structure, morphology and electrochemical performance.

2. Experimental section

2.1 Synthesis of cathode materials

The synthesis method used in this study was self-propagating combustion. The starting materials used in synthesising the undoped $LiNi_{0.6}Co_{0.3}Ti_{0.1}O_2$, novel nano-sized Al-doped $LiNi_{0.6}Co_{0.3-x}Al_xTi_{0.1}O_2$ and $LiNi_{0.6-x}Co_{0.3}Al_xTi_{0.1}O_2$ ($x = 0.01$) were metal nitrates, namely, lithium nitrate ($LiNO_3$), nickel(II) nitrate hexahydrate ($Ni(NO_3)_2 \cdot 6H_2O$), cobalt(II) nitrate hexahydrate ($Co(NO_3)_2 \cdot 6H_2O$), titanium nitrate ($Ti(NO_3)_4$) and aluminium(III) nitrate nonahydrate ($Al(NO_3)_3 \cdot 9H_2O$). Each of the starting materials was dissolved separately in deionised water to form several metal nitrate solutions. Next, a combusting agent, nitric acid (HNO_3), was dissolved in the deionised water. Once the starting materials were prepared, all of the dissolved starting material solutions were mixed into a larger beaker and stirred for 1 hour. After 1 hour, the mixture was heated at 250 °C (in the air) until it combusted to form a precursor after about 2 hours of heating. Then, the precursor was annealed at 700 °C in the air for 24 hours and the material obtained was ground to obtain the final product. The final products of undoped $LiNi_{0.6}Co_{0.3}Ti_{0.1}O_2$, novel nano-sized Al-doped $LiNi_{0.6}Co_{0.3-x}Al_xTi_{0.1}O_2$ and $LiNi_{0.6-x}Co_{0.3}Al_xTi_{0.1}O_2$ ($x = 0.01$) were denoted as LNCT, LCA and LNA, respectively.

2.2 Characterization

The phase and the purity of the synthesised materials were analysed using X-ray diffraction (XRD). The XRD data was obtained through a PANalytical Xpert Pro diffractometer with Cu Kα X-ray radiation for measurement over the 2θ range of 10–90°. The materials were measured using a Bragg–Brentano optical configuration with a spinning mode in order to minimise the preferred orientation effects. The quantitative XRD structural studies were analysed by the Rietveld refinement method as implemented in the X'pert Highscore Plus software.

As for morphological studies, the Field Emission Scanning Electron Microscopy (FESEM) coupled with an Energy Dispersive X-ray analyser (EDX) and High-Resolution Transmission Electron Microscopy (HRTEM) methods were used. The FESEM images were obtained using the JEOL JSM-7600F instrument while HRTEM JEOL JEM-2100F was the HRTEM instrument used in this study. With the help of these instruments, the morphology, crystallite size and lattice fringe of the samples were determined.

On the other hand, the chemical environments such as the oxidation states of the elements were determined with XPS using a JPS-9200 photoelectron spectrometer. The powdered sample was pressed into pellets for the XPS studies. Following pressing, the pellets were heated at 200 °C overnight in order to remove any unwanted surface hydrocarbons before being placed into the measurement chamber. The XPS spectra were then measured using a monochromator and Al K_α (1486 eV) radiation as the X-ray source. A charge neutraliser was used to minimise the charging effects. The pass energy of 10 eV was used to collect data. The data was analysed using JEOL Specsurf software and carbon peak value of 284.8 eV was used as a reference.

2.3 Electrochemical measurements

The fabrication of the cathode material was composed of 80% active materials (±0.023 mg weight loading), 10% carbon and 10% polytetrafluoroethylene (PTFE). The ingredients were mixed homogeneously and pressed onto a stainless-steel grid. Then, the fabricated cathode material was put into an oven and was dried at 200 °C for 24 hours. The dried fabricated cathode was then assembled together with the electrolyte, separator and the anode material under argon gas atmosphere inside a glove box (Mbraun Labmaster – Germany) for electrochemical performance testing. Li metal was used as the anode material and the electrolyte used was 1 M $LiPF_6$ in EC/DMC (1/1 v/v) from Mitsubishi Chemicals. The fabricated cathodes were assembled in a Teflon holder with coin cell configuration for battery testing. The electrochemical charge–discharge measurements were carried out using a WonaTech WBCS 3000 (Korea) battery tester, at a constant current of 1.0 mA and cycled at a voltage range of 2.5 to 4.3 V for 50 cycles.

3. Results and discussion

3.1 Phase and structural studies

Fig. 1 illustrates the XRD patterns of the LNCT, LCA and LNA. Referring to the XRD patterns, all samples displayed the single-phase, layered hexagonal α-$NaFeO_2$ structure with $R\bar{3}m$ space group, which is the same structure as $LiNiO_2$ with an ICDD database pattern number of 01-070-4310 accordingly.

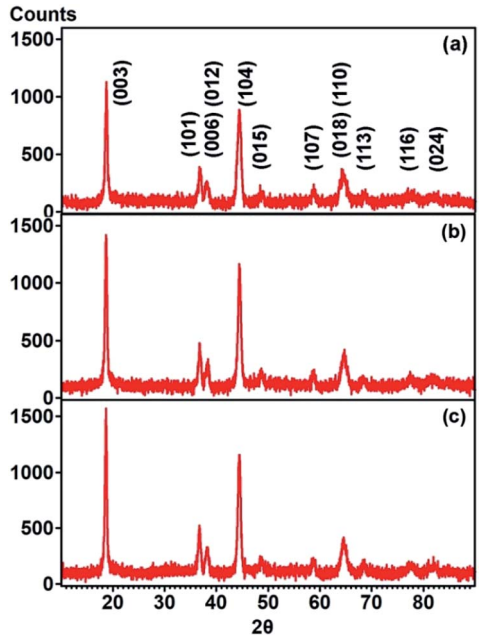

Fig. 1 XRD patterns of (a) LNCT (b) LCA (c) LNA annealed at 700 °C for 24 hours.

Therefore, it can be inferred that Al was successfully substituted in the LNCT crystal lattice. The degree of cation mixing in the structure was examined *via* the ratio of $I_{(003)/(104)}$ peak, RIR. The $I_{(003)/(104)}$ ratios estimated for LNCT, LCA and LNA were 1.15, 1.16 and 1.24, respectively. The LNA exhibited the highest $I_{(003)/(104)}$ ratio of 1.24, indicating that low cation mixing takes place between Li^+ ions at the 3b site and Ni^{2+} at the 3a site.[24] Therefore, it can be concluded that the decrease in cation mixing by replacing Al ions at the Ni site in the LNCT structure benefits the Li-ion diffusion. Using the XRD results, the mean crystallite size (D) of each sample was also identified using the Debye–Scherrer method as given in eqn (1):

$$D = \frac{k\lambda}{\beta \cos \theta} \quad (1)$$

where k is the shape factor, λ is the wavelength of the X-ray source, β is the full-width-at-half-maximum (FWHM) of the diffraction peak on a 2θ scale and θ is the Bragg angle. The Scherrer formula was applied to the three main XRD lines, namely (003), (101) and (104). The calculated mean crystallite sizes of LNCT, LCA and LNA were 19.64 nm, 17.33 nm and 13.74 nm, respectively, indicating that the Al-doped materials have a smaller crystallite size than the undoped material.

Further investigation into the crystal structure was carried out using the Rietveld refinement in order to obtain the lattice parameter. Based on the XRD patterns in Fig. 2(a)–(c), the XRD analysis was carried out at a higher count up to 10 000 and at a 2θ range up to 151°. The crystallographic parameters of LNCT, LCA and LNA materials extracted from Rietveld refinement are tabulated in Table 1. Referring to Table 1, the reasonably small

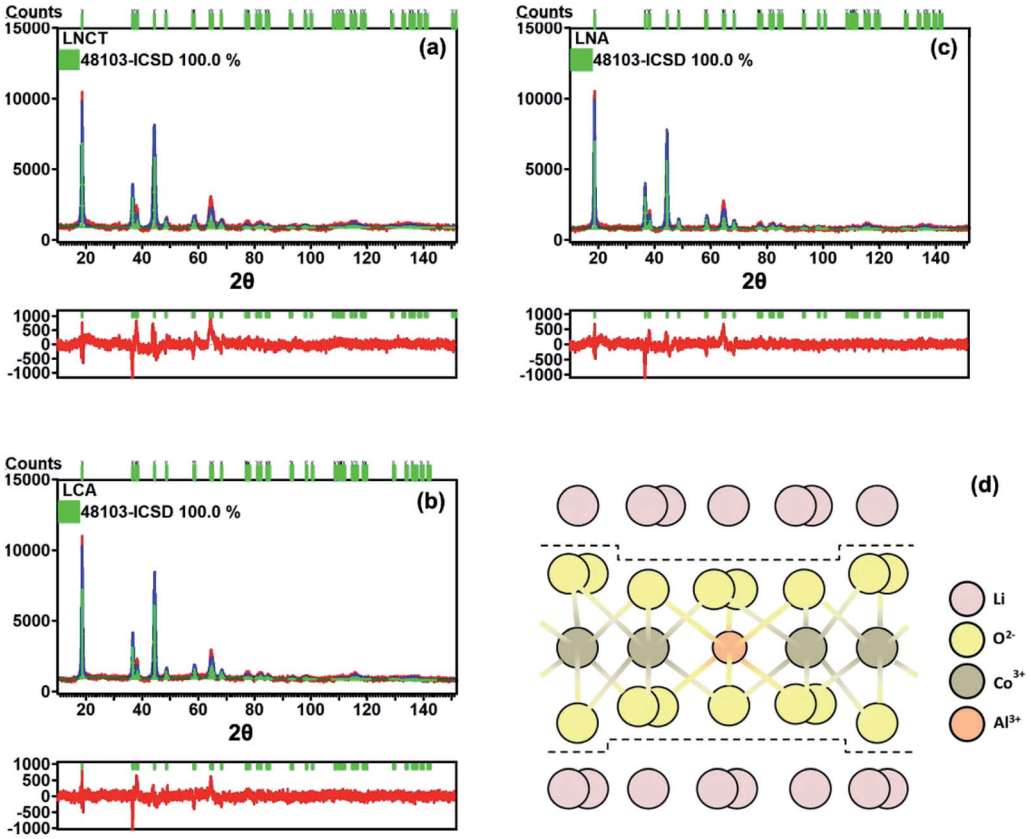

Fig. 2 Rietveld refinements of XRD patterns of (a) LNCT (b) LCA (c) LNA annealed at 700 °C for 24 hours and (d) illustration of Al doped into Co site of LNCT.

Table 1 Crystallographic parameters of LNCT, LCA and LNA materials (s.o.f. = site occupancy factor)

Sample	$a = b$ (Å)	c (Å)	V (Å^3)	c/a	R_w	s.o.f. of Li 3a	s.o.f. of Li 3b	s.o.f. of Ni 3b	s.o.f. of Ni 3a	s.o.f. of Co 3b	s.o.f. of Ti 3b	s.o.f. of Al 3b	s.o.f. of O 16c
LNCT	2.8772	14.3014	102.5261	4.9706	11.02	0.9760	0.0430	0.5662	0.0230	0.2903	0.0956	—	1.0000
LCA	2.8684	14.2418	101.4809	4.9651	8.23	0.9780	0.0430	0.5597	0.0210	0.2875	0.0967	0.0097	1.0000
LNA	2.8692	14.2416	101.5354	4.9636	9.36	0.9880	0.0250	0.5750	0.0120	0.2921	0.0973	0.0098	1.0000

Table 2 Atomic distances obtained from Rietveld refinements, stoichiometry of materials, RIR value and crystallite size obtained by Debye–Scherrer equation of the XRD results

Sample	Li–O (Å)	Li–TM (Å)	TM–O (Å)	RIR $I_{(003)/(104)}$	Stoichiometry of materials from XRD	Crystallite size using Debye–Scherrer equation (nm)
LNCT	2.120	2.905	1.974	1.15	$Li_{0.976}Ni_{0.566}Co_{0.290}Ti_{0.096}O_2$	19.64
LCA	2.114	2.894	1.966	1.16	$Li_{0.978}Ni_{0.560}Co_{0.288}Al_{0.010}Ti_{0.097}O_2$	17.33
LNA	2.119	2.894	1.962	1.24	$Li_{0.988}Ni_{0.575}Co_{0.292}Al_{0.010}Ti_{0.097}O_2$	13.74

values of weighted profile R-factor indicated that the proposed model is correct. The lattice parameters of LCA and LNA are smaller than those of LNCT. The substitution of Al^{3+} (0.535 Å) at Ni^{3+} (0.560 Å) or Co^{3+} (0.545 Å) sites allows the structure to become denser (smaller c value) due to the smaller ionic radius size of Al^{3+} compared to Ni^{3+} or Co^{3+}. An illustration of Al doped into Ni or Co sites of LNCT is shown in Fig. 2(d).

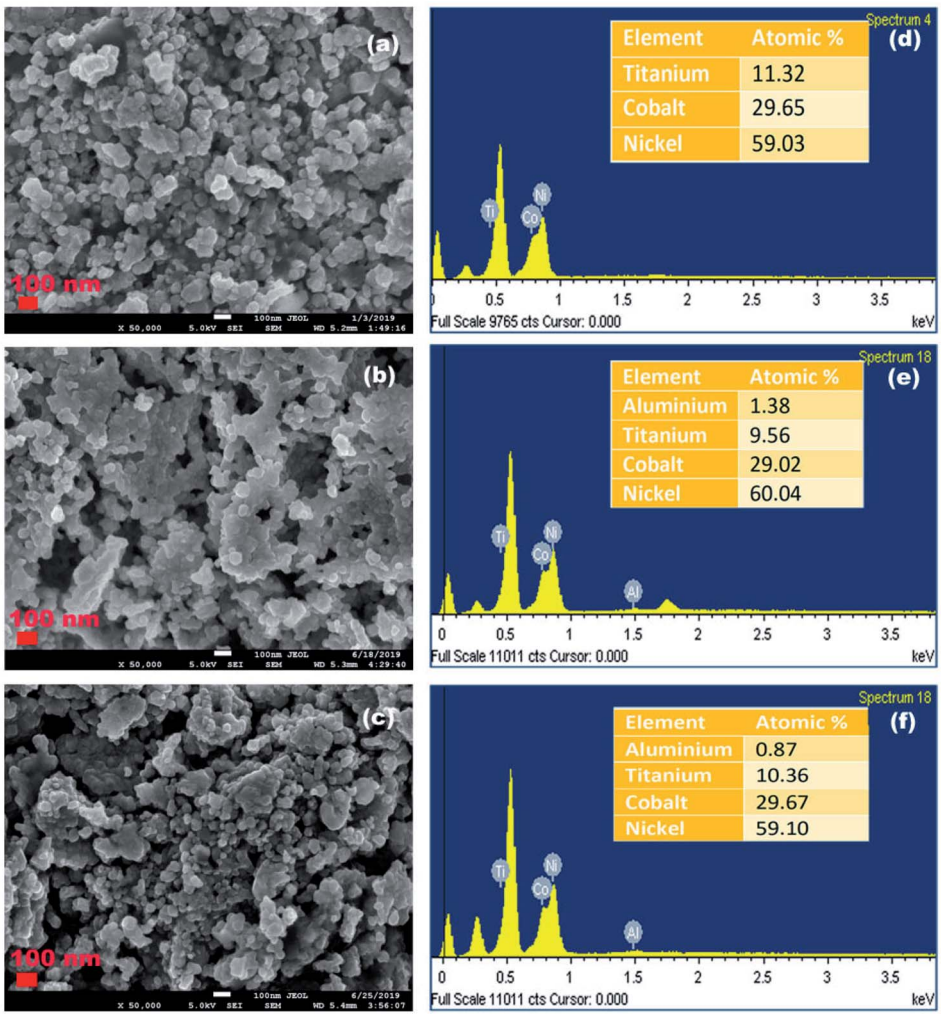

Fig. 3 FESEM images of (a) LNCT, (b) LCA and (c) LNA at 50k magnification while (d), (e) and (f) are their corresponding EDX spectra, respectively.

To further confirm the degree of Li^+/Ni^{2+} cation mixing in the pristine and doped samples, Rietveld refinement was performed to obtain the lattice parameter of the crystals. In Table 1, the Ni^{2+} at the 3a site for LNCT, LCA and LNA has a lattice parameter of 0.023, 0.021 and 0.012 respectively. The incorporation of Al^{3+} at a Ni or Co site reduced the cation mixing and among them, LNA has the lowest cation mixing. This implies that the substitution of Al^{3+} at the Ni site suppressed the Ni^{2+} ions from taking the place at the Li 3a site.

The atomic distances of Li–O, Li–TM and TM–O (where TM = transition metal) obtained from the Rietveld refinements are tabulated in Table 2. Based on the outcome, LCA and LNA samples have shorter atomic distances of Li–O, Li–TM and TM–O compared to those of LNCT. Since Al^{3+} has a smaller size than Co^{3+} and Ni^{3+}, Al^{3+} possesses smaller electron repulsion with the oxygen that surrounds the ions. As a result, oxygen will not be repelled as much as by the electron repulsion exhibited by Co^{3+} or Ni^{3+}.

Thus, the atomic distance between Al^{3+} with the surrounding oxygen becomes shorter and the crystal lattice becomes more stable due to the higher binding energy.[25] Short atomic distances translate to LCA and LNA having a smaller cell volume than LNCT. However, between LCA and LNA, the latter has a longer atomic distance of Li–O (interlayer slab). It was also found that the atomic distance of Li–O for the LNA sample is almost similar to the pristine sample, LNCT. This implies that the substitution of Al^{3+} at the Ni^{3+} site has suppressed the Ni^{2+} ions taking the place at the Li^+ 3a site in the interlayer slab. This finding is in agreement with Q. Zhang where the presence of Ni in Li slabs will reduce the interlayer distance, which then will increase the energy barrier for Li^+ ions to overcome during the delithiation/lithiation process and lead to the poor electrical performance.[26] Therefore, LNA is estimated to exhibit better electrochemical performance compared to LCA.

3.2 Morphology and elemental composition analysis

Fig. 3 shows the morphology of LNCT, LCA and LNA investigated using FESEM. All samples demonstrated polyhedral-like crystal shapes and as clearly evidenced, the doped samples possessed smaller crystallite sizes compared to a pristine sample. Therefore, the substitution of Al in the LNCT material is expected to reduce the crystallite size of the materials. The reduction of crystallite size translates to an increase in the contact area of the material. The increase in contact area will promote Li-ion exchange and increase the intercalation/

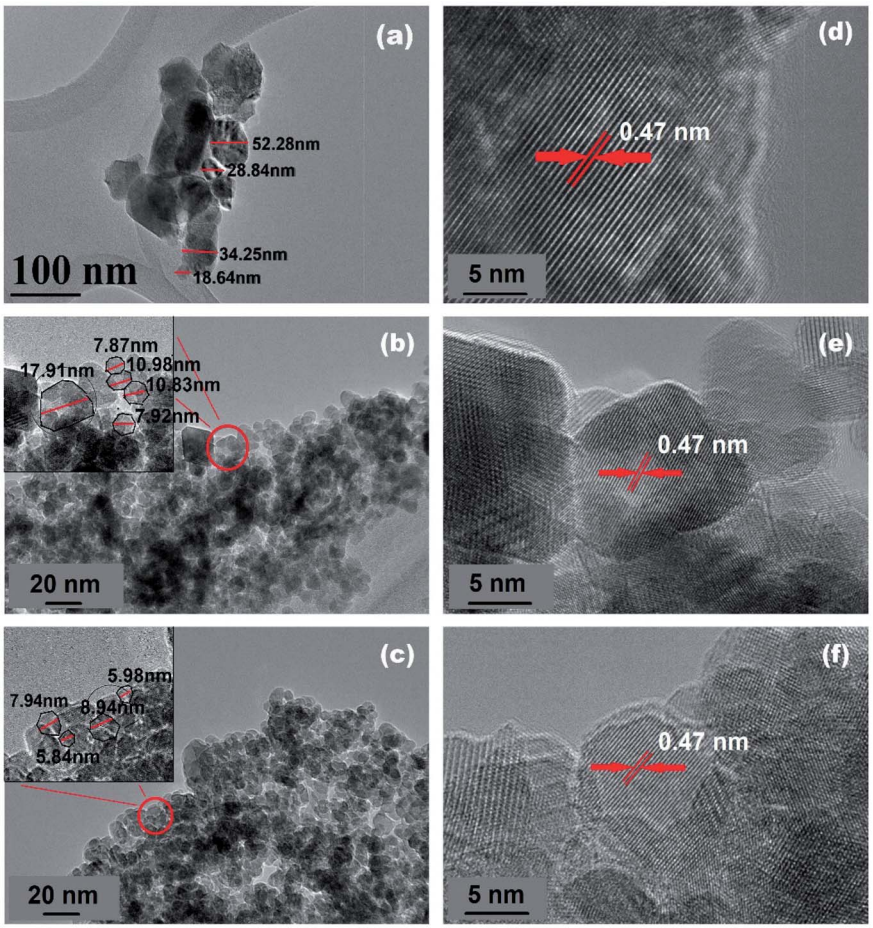

Fig. 4 HRTEM images of (a) LNCT at 40k magnification, (b) LCA and (c) LNA at 100k magnification while (d), (e) and (f) are their corresponding images at 800k magnification.

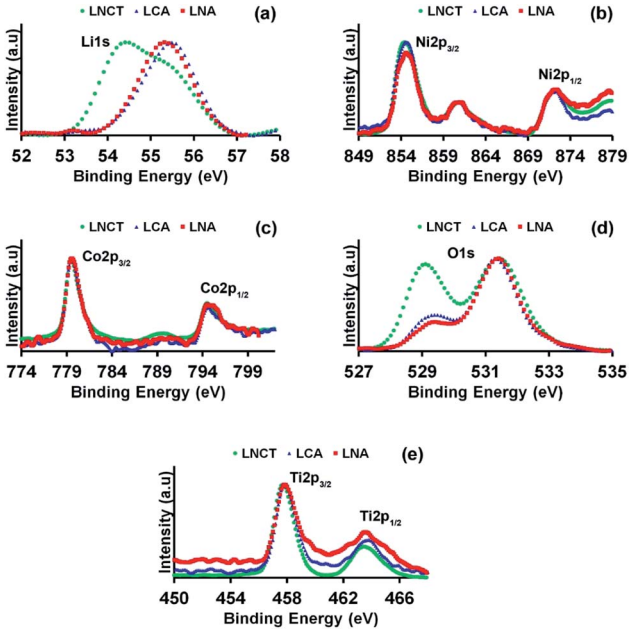

Fig. 5 XPS narrow scan spectra of (a) Li 1s (b) Ni 2p (c) Co 2p (d) O 1s and (e) Ti 2p of LNCT, LCA and LNA samples.

deintercalation rate of Li ions.[27] Thus, the cycling performance of the batteries will be improved with the increase in the intercalation/deintercalation rate of Li ions.

On the other hand, the elemental analysis was carried out using EDX to determine the experimental stoichiometries of all samples. Fig. 3(d)–(f) of the EDX results indicated that the atomic percentage of all elements in each of the samples were in good agreement with the atomic percentage obtained from the XRD Rietveld refinement. Similar elemental quantities between the experimental values with the calculated stoichiometry values implied that the samples were synthesised efficiently.

In addition, HRTEM was employed to illustrate the specific structure features of the LNCT, LCA and LNA samples (Fig. 4). Based on the results, both the Al-doped samples were observed to possess smaller crystallite sizes (range from 10–20 nm) compared to the undoped samples (range from 20–50 nm), as can be seen in Fig. 4(a)–(c), which is in agreement with the mean crystallite size calculated using the Debye–Scherrer formula (Table 2). Smaller crystallite sizes will benefit the delithiation/lithiation process by shortening Li-ion diffusion and increasing the contact area, which will promote the Li ion exchange resulting in improved electrochemical performance.[27] Moreover, Fig. 4(d)–(f) illustrate the lattice and diffraction patterns of the samples. According to the figures, all samples revealed clear lattice fringes with interplanar distances of 0.47 nm, which correspond to the (003) planes in the cathode materials.

3.3 Chemical environments assessment of elements *via* XPS

XPS analysis was performed to gain further information on the composition and the chemical states of the synthesised cathode

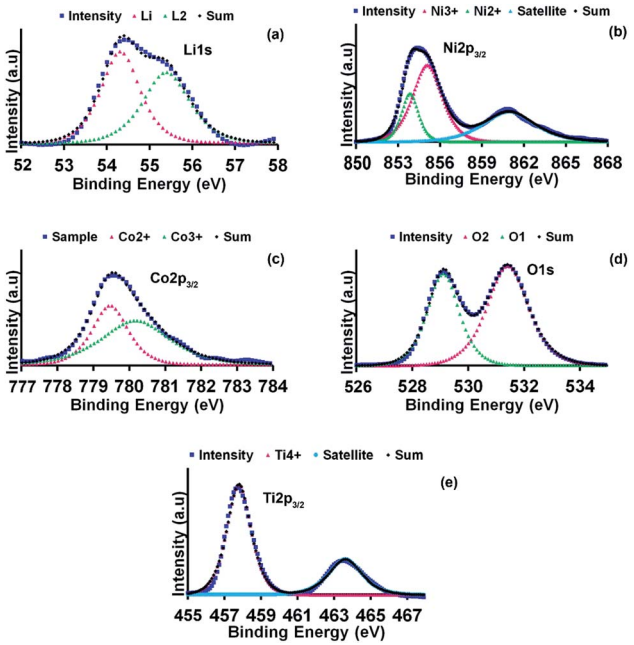

Fig. 6 The deconvolution of (a) Li 1s (b) Ni 2p (c) Co 2p (d) O 1s and (e) Ti 2p peaks for the LNCT sample.

Table 3 List of binding energy (B.E) and percentage ratio of oxidation states present in the cathode materials

		LNCT		LCA		LNA	
Component		Binding energy (eV)	Ratio	Binding energy (eV)	Ratio	Binding energy (eV)	Ratio
Li 1s	Li1	54.321	51.978	55.448	100	55.334	100
	Li2	55.392	48.022	—	—	—	—
Ni $2p_{3/2}$	Ni^{2+}	853.856	26.544	853.709	15.300	853.758	12.020
	Ni^{3+}	855.086	73.456	854.895	84.700	854.916	87.980
Co $2p_{3/2}$	Co^{2+}	779.545	46.400	779.472	50.264	779.466	41.424
	Co^{3+}	780.402	53.600	780.493	49.736	780.174	58.576
O 1s	O1	529.106	41.456	529.256	21.832	529.287	16.147
	O2	531.417	58.544	531.338	78.168	531.385	83.854
Ti $2p_{3/2}$	Ti^{4+}	457.790	100	457.936	100	458.004	100

materials. The XPS narrow scan spectra for all elements in LNCT, LCA and LNA samples are illustrated in Fig. 5. Unfortunately, the Al elements in LCA and LNA samples were undetected by XPS due to the low amounts of Al content (1%) in the samples. However, the presence of the Al in the synthesised samples was proven by the EDX results discussed earlier. The binding energy of the elements in all samples is tabulated in Table 3. Fig. 5(a) indicated that the Li 1s peak shifted to a higher binding energy position for doped samples compared to the undoped sample. The shift based on the Rietveld refinement results (Tables 1 and 2) postulated that the incorporation of Al in LNCT led to the shrinking of the structure to become more compact. Hence, the atomic position of the elements in the structure is closer to each other. Furthermore, the Li 1s peak for LNCT was asymmetrical, indicating the presence of more than one chemical environment for Li in the sample. Following the deconvolution of the Li 1s peak for the LNCT sample, there are two Li components consisting of one with a high binding energy (55.392 eV) due to the Li in the bulk sample and another with a low binding energy (54.321 eV) due to the dangling bonds of Li at the surface.[28] Meanwhile, for LNA and LCA samples, the Li 1s peak appeared symmetrical, indicating the presence of only one chemical environment for Li in the samples, which implies that the condition of Li on the surface and bulk are the same. The Ni, Co and Ti elements possess almost similar binding energies before and after Al-doped LNCT. Deconvolution of elements for LNCT is depicted in Fig. 6 as a representative for LCA and LNA samples. Further, the oxidation states for Ni and Co in all synthesised samples were in +2 and +3 states (Table 3). Moreover, the Ti existed as Ti^{4+} in all cathode materials. These values of binding energy are in agreement with other available literature.[3,29,30]

3.4 Electrochemical performance of cathode materials

Fig. 7 illustrates the charge–discharge capacity patterns, cyclability and C-rate of LNCT, LCA and LNA cathode materials. Additional details on the electrochemical performances of the three samples are tabulated in Table 4. Based on Table 4, the

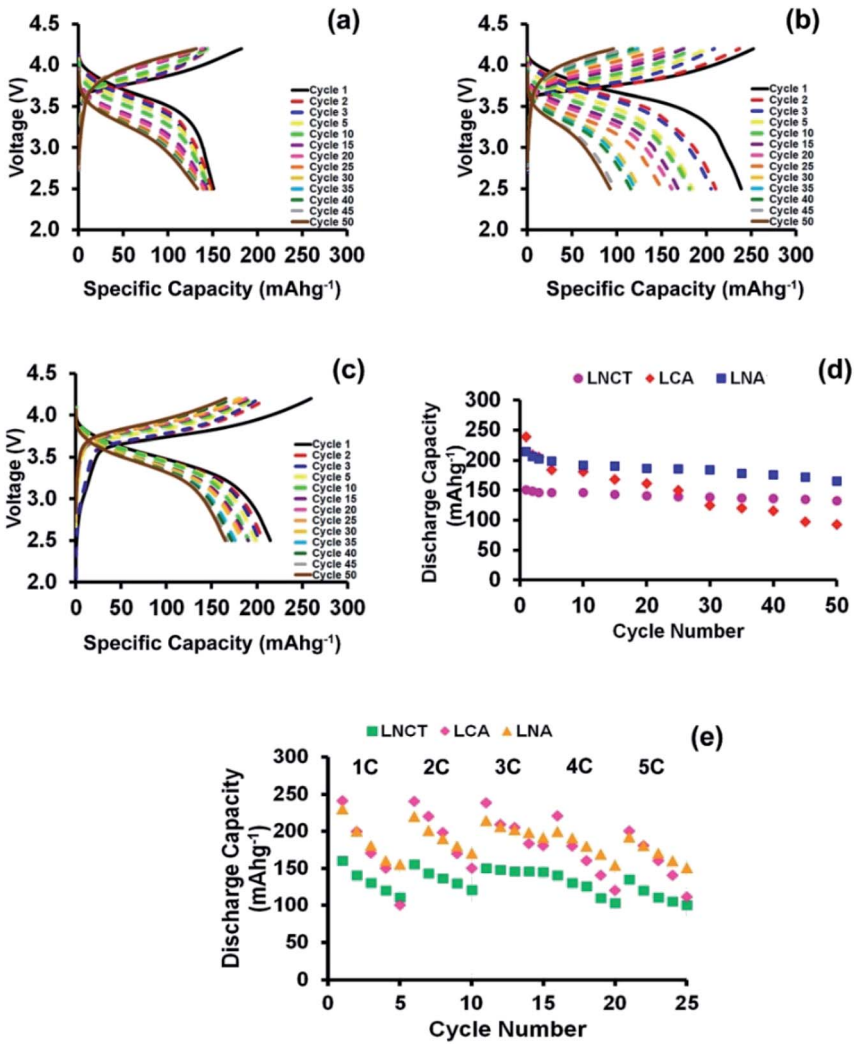

Fig. 7 Charge-discharged capacity of (a) LNCT, (b) LCA, (c) LNA for 50 cycles, (d) cyclability of LNCT, LCA, LNA and (e) comparison of cycling performances *vs.* C-rates.

Table 4 Electrochemical performance of LNCT, LCA and LNA for 50 cycles

	LNCT		LCA		LNA	
Cycle	Charge (mA h g^{-1})	Discharge (mA h g^{-1})	Charge (mA h g^{-1})	Discharge (mA h g^{-1})	Charge (mA h g^{-1})	Discharge (mA h g^{-1})
1^{st}	182.6	150.5	252.8	238.6	259.9	214.7
2^{nd}	147.5	148.1	238.0	209.0	211.2	206.6
3^{rd}	145.5	146.1	208.4	205.2	203.5	202.5
5^{th}	144.7	146.1	201.8	183.8	200.1	198.7
10^{th}	143.8	145.7	186.3	181.0	195.0	191.5
15^{th}	141.1	143.1	174.6	168.1	192.3	190.2
20^{th}	139.0	140.8	164.1	161.3	187.7	186.4
25^{th}	138.2	139.3	151.0	150.1	186.1	185.3
30^{th}	136.9	138.6	133.4	124.7	180.8	183.9
35^{th}	135.5	137.0	123.3	120.5	175.7	177.9
40^{th}	134.4	135.9	117.8	115.3	172.5	175.7
45^{th}	133.6	134.7	114.0	97.1	167.9	171.7
50^{th}	131.3	132.4	96.4	92.8	165.7	165.0
Capacity loss after 50^{th} cycle (%)	12.0		61.1		23.1	
Efficiency (%)	82.4		94.4		82.6	

initial discharge capacities of LNCT, LCA and LNA cathode materials were 150.5 mA h g^{-1}, 238.6 mA h g^{-1} and 214.7 mA h g^{-1}, respectively. It was also evident that doping Al into LNCT enhanced its specific capacity compared to undoped samples. LCA measured the highest initial discharged capacity (238.6 mA h g^{-1}) but it suffered a very high capacity decrease in the second cycle (12.4%) compared to LNCT and LNA (1.6% and 3.8%). Next, the coulombic efficiencies for LNCT, LCA and LNA were 82.4%, 94.4% and 82.6%, respectively. Upon reaching the 50^{th} cycle, the discharged capacity of LCA was the lowest among the three samples due to a high percentage of capacity fading (61.1%). This situation indicated the loss of numerous Li^+ ions during delithiation/lithiation, which may have been a result of the smaller Li–O atomic distances (Table 2). Smaller atomic distances between Li and O of the LCA sample make the lithiation of Li^+ ions difficult since it needs more energy to overcome the repulsion from the surrounding electrons compared to that of the LNCT and LNA samples.[3,31] Thus, the Li intercalation process becomes harder due to a higher energy resistance and the continuous loss of Li-ions that resulted in an increase in the capacity loss of the material.

In the meantime, LNA cathode materials recorded a lower capacity loss than the LCA sample at only 23.1% after the 50^{th} cycle. This low capacity loss was due to the longest Li–O atomic distance (Table 2) that makes the lithiation of Li^+ ions easier since there is less energy resistance from the surrounding electrons compared to LCA. Moreover, the shortest TM–O distance for the LNA sample proved that the more stable structure possesses excellent discharge capacity compared to the other samples. Therefore, even though LNA experiences a slightly higher-capacity loss upon the last cycle compared to LNCT (12.0%), LNA still generated the highest discharged capacity of 165.0 mA h g^{-1} upon the last cycle. Hence, the addition of Al at Ni sites in the LNCT structure helps in stabilising the cathode structure and improves the effectiveness of the intercalation process.

As for the rate capability of the materials, the graph of as-prepared LNCT, LCA and LNA are plotted accordingly. Graphs of 1C, 2C, 3C, 4C and 5C rates with 5 cycles representing each rate are shown in Fig. 7. Referring to Fig. 7(e), the discharge capacity of all materials decreased with increasing C-rate. However, at a 3C rate, all materials portray a more stable capacity, which means there is a low capacity loss as compared to 1C, 2C, 4C and 5C. Therefore, this study made use of the 3C rate for the entire electrochemical measurements.

4. Conclusions

In conclusion, improved, novel and nano-sized aluminium doped cathode materials were successfully synthesised. Al doped into $LiNi_{0.6}Co_{0.3-x}Ti_{0.1}O_2$ (LCA) or $LiNi_{0.6-x}Co_{0.3}Ti_{0.1}O_2$ (LNA) was proven to yield a higher initial discharged capacity than that of $LiNi_{0.6}Co_{0.3}Ti_{0.1}O_2$ (LNCT). However, LCA suffers a very high percentage of capacity loss (61.1%), resulting in worse performance upon the 50^{th} cycle. On the other hand, LNA was identified as an excellent cathode material since it can sustain up to 165.0 mA h g^{-1} upon the 50^{th} cycle because LNA has a long atomic distance of Li–O. The long atomic distance of Li–O will ease the diffusion of Li^+ ions, which requires less energy for the extraction of Li^+ ions from the material. In addition, the shortest TM–O distance for LNA improves the stability of the structure compared to the other samples, which contributes to the excellent discharge capacity.

Conflicts of interest

There are no conflicts of interest to declare.

Acknowledgements

The authors would like to acknowledge the Ministry of Higher Education of Malaysia for the financial support under the Fundamental Research Grant Scheme (FRGS/1/2017/STG01/

UITM/03/13) and Institute of Science, Universiti Teknologi MARA, Shah Alam, Malaysia for their support to this work in terms of instruments and materials used for the experiments.

References

1 U. P. Kumar and A. S. Nesaraj, *J. Nanotechnol. Adv. Mater.*, 2013, **86**, 75–86.
2 H. R. Kim, S. G. Woo, J. H. Kim, W. Cho and Y. J. Kim, *J. Electroanal. Chem.*, 2016, **782**, 168–173.
3 W. Zhao, M. Oyama, H. Yamada and H. Noguchi, *Electrochim. Acta*, 2015, **168**, 157–166.
4 B. Shen, Q. Liu, L. Wang, G. Yin, P. Zuo, Y. Ma, X. Cheng, C. Du and Y. Gao, *Electrochem. Commun.*, 2017, **83**, 106–109.
5 P. N. Kumta, D. Gallet, A. Waghray, G. E. Blomgren and M. P. Setter, *J. Power Sources*, 1998, **72**, 91–98.
6 A. Burukhin, O. Brylev, P. Hany and B. R. Churagulov, *Solid State Ionics*, 2002, **151**, 259–263.
7 A. Rougier, P. Gravereau and C. Delmas, *Electrochem. Soc. Proc. Ser.*, Pennington, NJ, 1993, vol. 143, pp. 1168–1175.
8 Y. Wang, J. Roller and R. Maric, *Electrochim. Acta*, 2017, **241**, 510–516.
9 R. Sathiyamoorthi, P. Santhosh, P. Shakkthivel and T. Vasudevan, *J. Solid State Electrochem.*, 2007, **11**, 1665–1669.
10 S. Madhavi, G. V. Subba Rao, B. V. R. Chowdari and S. F. Y. Li, *J. Power Sources*, 2001, **93**, 156–162.
11 C. Song, W. Wang, H. Peng, Y. Wang, C. Zhao, H. Zhang, Q. Tang, J. Lv, X. Du and Y. Duo, *Appl. Sci.*, 2018, **8**, 378.
12 H. S. Ko, J. H. Kim, J. Wang and J. D. Lee, *J. Power Sources*, 2017, **372**, 107–115.
13 P. B. Samarasingha, A. Wijayasinghe, M. Behm, L. Dissanayake and G. Lindbergh, *Solid State Ionics*, 2014, **268**, 226–230.
14 A. E. Abdel-Ghany, A. M. Hashem, E. A. Elzahany, H. A. Abuzeid, S. Indris, K. Nikolowski, H. Ehrenberg, K. Zaghib, A. Mauger and C. M. Julien, *J. Power Sources*, 2016, **320**, 168–179.
15 S. T. Myung, F. Maglia, K. J. Park, C. S. Yoon, P. Lamp, S. J. Kim and Y. K. Sun, *ACS Energy Lett.*, 2017, **2**, 196–223.
16 D. Y. Wan, Z. Y. Fan, Y. X. Dong, E. Baasanjav, H. B. Jun, E. M. Jin and S. M. Jeong, *J. Nanomater.*, 2018, **2018**, 1–9.
17 D. Baster, P. Paziak, M. Zi, G. Wazny and J. Molenda, *Solid State Ionics*, 2018, **320**, 118–125.
18 D. D. K. Ghatak, S. Basu, T. Das and H. Kumar, *Phys. Chem. Chem. Phys.*, 2018, **20**, 22805–22817.
19 Y. Huang, Y. Huang and X. Hu, *Electrochim. Acta*, 2017, **231**, 294–299.
20 P. Sun, Y. Ma, T. Zhai and H. Li, *Electrochim. Acta*, 2016, **191**, 237–246.
21 K. Elong, N. Kamarulzaman, R. Rusdi, N. Badar and M. H. Jaafar, *Int. Scholarly Res. Not.*, 2013, **2013**, 1–8.
22 C. L. Yeh, *Ref. Modul. Mater. Sci. Mater. Eng.*, 2016, pp. 1–8.
23 W. Wen, J. Yao, C. Jiang and J. Wu, *Int. J. Self-Propag. High-Temp. Synth.*, 2017, **26**, 187–198.
24 L. Peng, Y. Zhu, U. Khakoo and G. Yu, *Nano Energy*, 2015, **17**, 36–42.
25 Y. P. Zhang, E. Q. Liang, J. X. Wang, B. J. Yu, C. Y. Wang and M. W. Li, *Int. J. Electrochem. Sci.*, 2017, **12**, 9051–9060.
26 Q. Zhang, Y. Su, L. Chen, Y. Lu, L. Bao, T. He, J. Wang, R. Chen, J. Tan and F. Wu, *J. Power Sources*, 2018, **396**, 734–741.
27 H.-R. Yao, Y.-X. Yin and Y.-G. Guo, *Chin. Phys. B*, 2016, **25**, 018203.
28 N. Kamarulzaman, A. Azahidi, K. Elong, M. F. Kasim, R. Rusdi, N. A. M. Mokhtar, N. D. A. Aziz and Z. Osman, *Mater. Res. Express*, 2017, **4**(4), 046301.
29 R. Qiao, J. Liu, K. Kourtakis, M. G. Roelofs, D. L. Peterson, J. P. Duff, D. T. Deibler, L. A. Wray and W. Yang, *J. Power Sources*, 2017, **360**, 294–300.
30 J. Zhang, R. Gao, L. Sun, H. Zhang, Z. Hu and X. Liu, *Electrochim. Acta*, 2016, **209**, 102–110.
31 T. F. Yi, J. Mei and Y. R. Zhu, *J. Power Sources*, 2016, **316**, 85–105.